

7-7-2020

## On the elastic anisotropy of the entropy-stabilized oxide (Mg, Co, Ni, Cu, Zn)O compound

Krishna Chaitanya Pitike  
*Oak Ridge National Laboratory*

Andres E. Marquez-Rossy  
*Oak Ridge National Laboratory*

Alexis Flores-Betancourt  
*Oak Ridge National Laboratory*

De Xin Chen  
*Oak Ridge National Laboratory*

Santosh KC  
*San Jose State University, santosh.kc@sjsu.edu*

*See next page for additional authors*

Follow this and additional works at: [https://scholarworks.sjsu.edu/faculty\\_rsca](https://scholarworks.sjsu.edu/faculty_rsca)

---

### Recommended Citation

Krishna Chaitanya Pitike, Andres E. Marquez-Rossy, Alexis Flores-Betancourt, De Xin Chen, Santosh KC, Valentino R. Cooper, and Edgar Lara-Curzio. "On the elastic anisotropy of the entropy-stabilized oxide (Mg, Co, Ni, Cu, Zn)O compound" *Journal of Applied Physics* (2020). <https://doi.org/10.1063/5.0011352>

This Article is brought to you for free and open access by SJSU ScholarWorks. It has been accepted for inclusion in Faculty Research, Scholarly, and Creative Activity by an authorized administrator of SJSU ScholarWorks. For more information, please contact [scholarworks@sjsu.edu](mailto:scholarworks@sjsu.edu).

---

**Authors**

Krishna Chaitanya Pitike, Andres E. Marquez-Rossy, Alexis Flores-Betancourt, De Xin Chen, Santosh KC, Valentino R. Cooper, and Edgar Lara-Curzio

# On the elastic anisotropy of the entropy-stabilized oxide (Mg, Co, Ni, Cu, Zn)O compound <sup>EP</sup>

Cite as: J. Appl. Phys. **128**, 015101 (2020); <https://doi.org/10.1063/5.0011352>

Submitted: 20 April 2020 • Accepted: 14 June 2020 • Published Online: 01 July 2020

 Krishna Chaitanya Pitike, Andres E. Marquez-Rossy, Alexis Flores-Betancourt, et al.

## COLLECTIONS

 This paper was selected as an Editor's Pick



View Online



Export Citation



CrossMark

## ARTICLES YOU MAY BE INTERESTED IN

The emergent field of high entropy oxides: Design, prospects, challenges, and opportunities for tailoring material properties

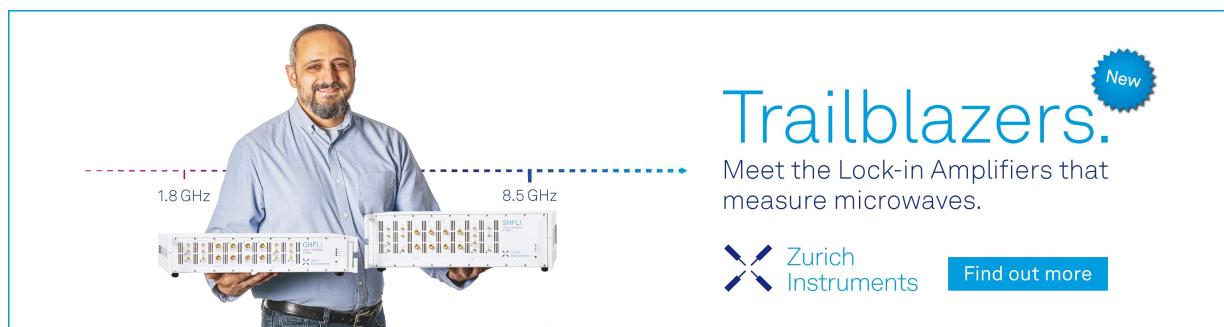
APL Materials **8**, 040912 (2020); <https://doi.org/10.1063/5.0003149>

Exchange interactions and long-range magnetic order in the (Mg,Co,Cu,Ni,Zn)O entropy-stabilized oxide: A theoretical investigation

Journal of Applied Physics **127**, 185108 (2020); <https://doi.org/10.1063/5.0008258>

Long-range magnetic ordering in rocksalt-type high-entropy oxides

Applied Physics Letters **114**, 122401 (2019); <https://doi.org/10.1063/1.5091787>



**Trailblazers.** <sup>New</sup>

Meet the Lock-in Amplifiers that measure microwaves.

Zurich Instruments [Find out more](#)

# On the elastic anisotropy of the entropy-stabilized oxide (Mg, Co, Ni, Cu, Zn)O compound

Cite as: J. Appl. Phys. 128, 015101 (2020); doi: 10.1063/5.0011352

Submitted: 20 April 2020 · Accepted: 14 June 2020 ·

Published Online: 1 July 2020



Krishna Chaitanya Pitike,<sup>1</sup>  Andres E. Marquez-Rossy,<sup>1</sup> Alexis Flores-Betancourt,<sup>1</sup> De Xin Chen,<sup>1</sup> KC Santosh,<sup>2</sup> Valentino R. Cooper,<sup>1</sup>  and Edgar Lara-Curzio<sup>1,a)</sup> 

## AFFILIATIONS

<sup>1</sup>Materials Science and Technology Division, Oak Ridge National Laboratory, 1 Bethel Valley Rd., Oak Ridge, Tennessee 37831, USA

<sup>2</sup>Chemical and Materials Engineering, San José State University, San José, California 95112, USA

<sup>a)</sup>Author to whom correspondence should be addressed: [laracurzioe@ornl.gov](mailto:laracurzioe@ornl.gov)

## ABSTRACT

In this paper, we study the elastic properties of the entropy-stabilized oxide (Mg, Co, Ni, Cu, Zn)O using experimental and first principles techniques. Our measurements of the indentation modulus on grains with a wide range of crystallographic orientations of the entropy-stabilized oxide revealed a high degree of elastic isotropy at ambient conditions. First principles calculations predict mild elastic anisotropy for the paramagnetic structure, which decreases when the system is considered to be non-magnetic. When the antiferromagnetic state of CoO, CuO, and NiO is accounted for in the calculations, a slight increase in elastic anisotropy is observed, suggesting a coupling between magnetic ordering and the orientation dependent elastic properties. Furthermore, an examination of the local structure reveals that the isotropy is favored through local ionic distortions of Cu and Zn—due to their tendencies to form tenorite and wurtzite phases. The relationships between the elastic properties of the multicomponent oxide and those of its constituent binary oxides are reviewed. These insights open up new avenues for controlling isotropy for technological applications through tuning composition and structure in the entropy-stabilized oxide or the high-entropy compounds in general.

Published under license by AIP Publishing. <https://doi.org/10.1063/5.0011352>

## I. INTRODUCTION

Elastic anisotropy is known to affect phonon modes,<sup>1</sup> phase transformations,<sup>2</sup> dislocation dynamics,<sup>3</sup> crack propagation,<sup>4</sup> charge defect mobility,<sup>5</sup> among many other processes. Hence, elastic anisotropy has been a property of interest to the research community studying mechanical and related physical properties of materials. Understanding the influence of mixing several chemical species—for example, a high-entropy compound—on elastic anisotropy is of paramount importance for engineering new high-entropy materials for mechanical applications.

Since the discovery of a multicomponent entropy stabilized oxide in the rock salt phase,<sup>6</sup> there has been a surge in the design and synthesis of entropy-stabilized compounds. These include perovskite oxides,<sup>7–9</sup> fluorites,<sup>10,11</sup> spinel,<sup>12</sup> boride,<sup>13</sup> and carbides.<sup>14–18</sup> Early reports indicate many interesting emergent properties, such as long range magnetic ordering,<sup>19</sup> reversible energy storage,<sup>20</sup> and giant exchange-coupling enhancement.<sup>21</sup> However, the role of chemical disorder on the physical and chemical properties of the entropy stabilized material is not well understood. Another key question is

how does the behavior of an entropy-stabilized material differ from that of its end-member components? Here, we explore the linear elastic properties of the Entropy-Stabilized Oxide—(Mg, Co, Ni, Cu, Zn)O, henceforth denoted as simply ESO—stabilized in the rock salt phase. Specifically, we report on anisotropy in elastic properties of the ESO using both first principles computations and experimental measurements.

The first work to address the importance of quantifying anisotropy was by Zener<sup>22</sup> in 1930. In his work, Zener proposed the following parameter to quantify the anisotropy of cubic crystals:<sup>22</sup>

$$A^Z = \frac{2(s_{11} - s_{12})}{s_{44}} = \frac{2c_{44}}{c_{11} - c_{12}}, \quad (1)$$

where  $s_{ij}$  and  $c_{ij}$  refer to compliance and stiffness constants of the material, respectively. Zener's anisotropy factor represents the ratio of the two extreme elastic shear coefficients in a cubic crystal:  $c_{44}$  representing resistance to shear on {100} in the  $\langle 0kl \rangle$  direction and  $(c_{11} - c_{12})/2$  representing resistance to shear on {110} in the

(110) direction.<sup>22</sup> When a cubic crystal is isotropic,  $A^Z = 1$  and deviations from unity are indicative of the degree of anisotropy. In most cases,  $A^Z > 1$ , but there are bcc crystals, such as polonium and some oxide fluorites and halides, for which  $A^Z < 1$ .<sup>23,24</sup>

Later, Ranganathan and Ostoja-Starzewski derived an elastic anisotropy index  $A^U$  to provide a measure of elastic anisotropy regardless of the symmetry of the crystal.<sup>25</sup> This parameter is based on the fractional difference between the upper and lower bounds on the bulk and shear moduli according to the following relationship:

$$A^U = 5 \frac{G^V}{G^R} + \frac{K^V}{K^R} - 6, \quad (2)$$

where  $G$  and  $K$  are the shear and bulk moduli, respectively, and  $V$  and  $R$  correspond to the Voigt (upper bound) and the Reuss (lower bound) estimates, respectively. For isotropic crystals,  $A^U$  is equal to zero, and the extent of anisotropy is defined by the departure of  $A^U$  from zero.<sup>25</sup>

Here, we show that the ESO exhibits a high degree of elastic isotropy through indentation modulus measurements and first principles estimated elastic properties. We find that the elastic properties, such as the anisotropy index and bulk and shear moduli, are well represented by a linear combination of the respective properties of the parent binary oxides. Through first principles calculations, we probe the influence of the local structure and magnetic configuration on elastic anisotropy. Specifically, we find that the local distortions around Cu and Zn cations in the nonmagnetic structure—as a result of their tendencies to form tenorite and wurtzite phases—promote isotropy. However, we find increasing degrees of elastic anisotropy in the paramagnetic and antiferromagnetic phases due to the suppressed local distortions and magnetic anisotropy in the antiferromagnetic structure. Antiferromagnetic ordering is only observed below the Néel temperature  $T_N = 113$  K,<sup>19</sup> suggesting a strong temperature dependence of elastic isotropy due to a magnetic phase transition. Similarly, the mixed phase to single phase transition at high temperature may also induce reduction in anisotropy at higher temperature. Together these results present a large phase space through which the elastic properties of ESO may be tuned and thus have implications for its use in different applications.

## II. EXPERIMENTAL

### A. Sample

The material used in this investigation was obtained by consolidating mixed oxide powders prepared by the polymerized organic-inorganic route.<sup>26</sup> The powders were hot-pressed at 1100 °C for 3 h under a compressive stress of 55 MPa.

The chemical composition, microstructure, crystal structure, and crystal orientation of the consolidated ESO material were determined by scanning electron microscopy, electron dispersive spectroscopy, x-ray diffraction, and electron backscatter diffraction (EBSD). Details about the characterization of the material are provided as [supplementary material](#).

### B. Indentation

Several arrays of  $20 \times 20$  nanoindenters were made on grains with different crystallographic orientations using a nanoindenter equipped with a Berkovich diamond indenter. The indentation modulus,  $M$ , was calculated from the experimentally determined reduced modulus,  $M_r$ , according to the following relationship:<sup>27</sup>

$$\frac{1}{M} = \frac{1}{M_r} - \left( \frac{1 - \nu_i^2}{E_i} \right), \quad (3)$$

where  $\nu_i = 0.07$  and  $E_i = 1.141$  GPa are Poisson's ratio and Young's modulus of the diamond indenter, respectively [TI 950 TribolIndenter User Manual Revision 9.3.0314, Hysitron Incorporated (2014)].

The indentation modulus  $M(hkl)$  of the  $(hkl)$  surface of a single crystal can be predicted as the product of a correction factor  $\beta_{hkl}$  and the indentation modulus of an isotropic, randomly oriented, polycrystalline aggregate of the same material,<sup>27</sup>

$$M_{hkl} = \alpha \beta_{hkl} \left( \frac{E}{1 - \nu^2} \right)_{\text{isotropic}}, \quad (4)$$

where  $\alpha$  is an additional correction factor to account for the geometry of the indenter tip and its orientation with respect to the crystallographic orientation of the indented surface. The correction factor  $\beta_{hkl}$  for crystals with cubic symmetry is given by

$$\beta_{hkl} = a + c(Z - A_0)^B, \quad (5)$$

where  $a$ ,  $c$ ,  $A_0$ , and  $B$  are the functions of Poisson's ratio in the cube directions.<sup>27</sup> The indentation modulus of the isotropic, randomly oriented, polycrystalline aggregate can be determined using the Voigt–Reuss–Hill average that is calculated using the elastic constants of a single crystal.<sup>28</sup> Additional details are presented in the [supplementary material](#).

### C. Theoretical and computational details

First principles calculations were performed using density functional theory (DFT) as implemented in the Vienna Ab initio Simulation Package (VASP)<sup>29,30</sup> with Perdew–Burke–Ernzerhof for solids (PBEsol) spin density approximation<sup>31</sup> for exchange correlation. The projector-augmented plane-wave method<sup>32,33</sup> with a 600 eV energy cutoff was used. For a primitive unit cell in the rock salt phase containing two atoms, a zone-edge-shifted  $8 \times 8 \times 8$  automatically generated k-point mesh was used for Brillouin zone (BZ) integrations. For the larger supercells required for modeling the ESO—containing 160 atoms—a  $\Gamma$  point calculation was done. In all DFT calculations, internal ionic positions were relaxed to forces less than 0.005 eV/Å. The lattice constants were relaxed until the appropriate stress tensor components were less than 0.1 kbar.

To account for the Coulomb interactions within the partially filled  $d$ -orbitals of the Co, Ni, and Cu cations in their respective binary oxides and also the ESO, we employ the DFT+ $U$  approach using the simplified (rotationally invariant) approach.<sup>34</sup>  $U = 6$  eV

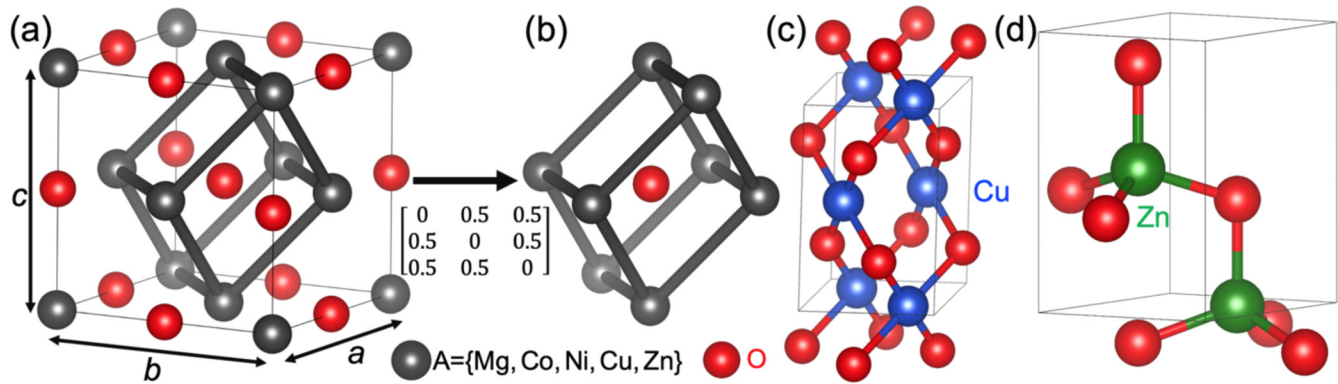


**FIG. 1.** (a) Face centered cubic structure of the rock salt phase with four lattice points of entropy stabilized oxide. (b) Primitive cell of the rock salt structure with four lattice points obtained from the rotation matrix shown near arrow. A-site is quasi-randomly occupied with equal probability by Mg, Co, Ni, Cu, and Zn. A  $4 \times 4 \times 5$  supercell of the primitive cell containing 160 atoms was used to model the ESO. (c) Tenorite and (d) wurtzite structures.

was used for Co, Ni, and Cu *d*-states, in order to find the stable ground phases of their respective binary oxides—the rock salt phase for CoO, NiO, and Tenorite phase for CuO. Furthermore, CoO, NiO, and the antiferromagnetic (AFM) model of ESO were initialized to an antiferromagnetic (AFM) ordering state with ferromagnetic planes parallel to (111) planes.

Figures 1(a) and 1(b) show the rock salt structure in the  $Fm\bar{3}m$  space group with 4 and 1 AO formula units per unit cells, respectively. The primitive unit cell (PC) was obtained from the FCC unit cell by the rotation matrix shown below the arrow. The ESO is modelled using a  $4 \times 4 \times 5$  supercell of PC where  $A = 0.2 \times \{\text{Mg, Co, Ni, Cu, Zn}\}$ . The five cations are quasi-randomly assigned to the A-site using the special quasi-random structures algorithm introduced by Zunger *et al.*<sup>35</sup> and implemented in Alloy Theoretic Automated Toolkit (ATAT) open source software.<sup>36</sup> The lattice constants for the constituent binary oxide and ESO models in their respective ground phases are compared with experimental values in Table SIII in the [supplementary material](#). Moreover, the lattice constants for CuO and ZnO are also provided in the rock salt phase.

The linear elastic stiffness coefficients were calculated from DFT using a method similar to that used for calculating the elastic constants presented in the Materials Project (MP).<sup>37,38</sup> Details can be found in the [supplementary material](#). Values of the Néel temperature,  $T_N$ , of CoO, NiO, CuO, and ESO have been experimentally determined as 291 K, 525 K, 220 K, and 113 K, respectively.<sup>19,39,40</sup> The predicted values of Young's modulus of the ESO in this work are compared with experimental values determined at room temperature,  $RT \sim 300$  K. Therefore, since the value of  $T_N$  for the ESO compound,  $T_N^{\text{ESO}} < RT$ , there should be no magnetic ordering in the ESO. Furthermore, the paramagnetic (PM) behavior has also been observed from the linear behavior of the magnetization measurements at RT.<sup>19</sup> Hence, the stiffness constants of the ESO were determined in the paramagnetic phase (Co, Ni, and Cu ions are randomly populated with positive and negative moments with net magnetic moment = 0) and the nonmagnetic (NM) phase (individual moments on Co, Ni, and Cu ions = 0). The stiffness constants of the ESO in the AFM ordered phase were also determined

for reference. Similarly, in the case of CuO,  $T_N^{\text{CuO}} < RT$ , we determined the elastic constants of CuO in the nonmagnetic rock salt phase. CuO in the tenorite phase with AFM ordering at low temperature were also determined for comparison, while the stiffness constants of NiO and CoO were determined in the AFM ordered rock salt phase.

### III. RESULTS AND DISCUSSION

Figure 2 shows the measured indentation modulus as a function of  $l_1^2 l_2^2 + l_1^2 l_3^2 + l_2^2 l_3^2$ , where  $l_i$  are the direction cosines. Each data point corresponds to the average of all indents obtained within a given grain. The error bars correspond to one standard deviation about the mean value. Two datasets are included in the plot for peak indentation loads of 2 and 5 mN. A regression analysis of the results indicates that the indentation modulus is effectively independent of crystallographic orientation. Also included in Fig. 2 are Young's modulus estimated from DFT calculations and estimated values for the indentation modulus from first principles according to the formulation of Vlassak and Nix for grains oriented in the [100], [110], and [111] directions. Details of the data analysis are included in the [supplementary material](#). The blue, red, and black lines correspond to the DFT-estimated Young's modulus for antiferromagnetic, paramagnetic, and nonmagnetic structures, respectively. The elastic constants for the paramagnetic structure were obtained from Boltzmann average of two different random structures. Refer to the Sec. II of the [supplementary material](#) for the detailed method of determining elastic constants and Young's modulus. The magnitude of the predicted Young's modulus was found to be greater than the experimentally determined indentation modulus. It has been found that among the various techniques available for measuring Young's modulus, nanoindentation usually has the lowest precision<sup>41</sup> and that differences between measured and estimated values of Young's modulus can vary by as much as 20%. It is believed that the precision of the nanoindentation measurement contributed to these discrepancies. Furthermore, we find that the predicted elastic constants for the parent oxides were generally

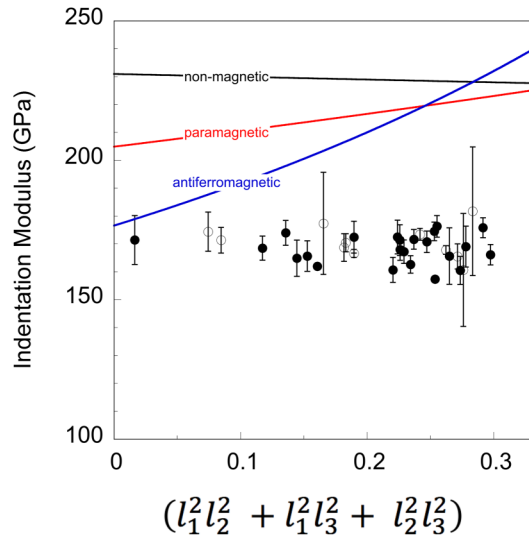


**FIG. 2.** Indentation modulus of (Mg, Co, Ni, Cu, Zn)O entropy stabilized oxide as a function of crystallographic orientation. The two datasets correspond to peak loads of 2 and 5 mN. Data points correspond to average values from measurements on individual grains. The crystallographic orientation of each grain was determined using electron backscatter diffraction. The blue, red, and black lines correspond to the DFT-estimated Young's modulus for antiferromagnetic, paramagnetic, and nonmagnetic structures, respectively.

greater than those measured experimentally. Refer to Table SIV in the [supplementary material](#) for a comprehensive list of experimentally determined elastic stiffness constants ( $c_{ij}$ ), anisotropy factors ( $A^Z, A^U$ ), Young's modulus ( $E$ ), Poisson's ratio ( $\nu$ ), and bulk and shear modulus ( $K, G$ ) of constituent binary oxides.<sup>37,38,42-49</sup>

To better understand the measured isotropic behavior, we employed first principles calculations to predict the elastic constants for the binary oxides and the ESO. [Table I](#) lists calculated values for stiffness constants,  $c_{ij}$ ; bulk modulus,  $K_{VRH}$ ; shear modulus,  $G_{VRH}$ ; elastic modulus,  $E$ ; Poisson's ratio,  $\nu$ ; Zener anisotropy ratio,  $A^Z$ ; and universal anisotropy ratio,  $A^U$ . Refer to [Sec. II](#) and [Table SII](#) in the [supplementary material](#) for detailed discussion on the method of estimation of the elastic constants from the first principles. For consistency in the comparison of elastic properties between the constituent binary oxides and the ESO, calculations were performed for CuO and ZnO in the rock salt structure. In all cases we studied, including the AFM, NM and PM structures, the following relations hold:

$$c_{44} > 0,$$

$$c_{11} > |c_{12}|,$$

$$c_{11} + 2c_{12} > 0,$$

which are conditions for mechanical stability for cubic crystals.<sup>50</sup>

**TABLE I.** Values of elastic constants, bulk modulus, shear modulus, Young's modulus, Poisson's ratio, Zener anisotropy ratio, and universal anisotropy ratio for individual binary oxides and ESO. Reference [0] corresponds to this work.

Compound	Phase	Reference	Method	$c_{11}$	$c_{12}$	$c_{44}$	$K_{VRH}$	$G_{VRH}$	$E$	$\nu$	$A^Z$	$A^U$
				$c_{22}$	$c_{23}$	$c_{55}$						
				$c_{33}$	$c_{31}$	$c_{66}$						
MgO	Rock salt-NM	[0]	DFT; U = 0	289.53	86.37	136.10	154.09	121.05	287.80	0.19	1.34	0.10
CoO	Rock salt-NM	[0]	DFT; U = 0	395.00	191.00	36.00	259.00	55.49	155.36	0.40	0.35	1.42
CoO	Rock salt-AFM	[0]	DFT; U = 0	313.37	146.36	59.81	202.03	68.38	184.34	0.35	0.72	0.14
CoO	Rock salt-AFM	[0]	DFT; U = 6	313.36	124.81	85.36	187.66	88.82	230.15	0.30	0.91	0.01
NiO	Rock salt-NM	[0]	DFT; U = 0	360.00	205.00	36.00	256.67	49.21	138.75	0.41	0.47	0.74
NiO	Rock salt-AFM	[0]	DFT; U = 0	389.16	131.56	43.09	217.47	68.05	184.86	0.36	0.34	1.59
NiO	Rock salt-AFM	[0]	DFT; U = 6	415.72	117.97	91.69	217.22	111.45	285.51	0.28	0.62	0.29
CuO	Rock salt-NM	[0]	DFT; U = 0	254.00	183.00	50.00	206.67	43.59	122.18	0.40	1.41	0.14
CuO	Tenorite-AFM	[0]	DFT; U = 0	154.44	144.77	67.82	159.73	21.62	62.07	0.44	...	11.81
				151.31	143.84	8.13						
				367.83	143.60	9.91						
CuO	Tenorite-AFM	[0]	DFT; U = 6	295.68	152.58	100.65	140.87	46.77	126.32	0.35	...	4.12
				126.74	85.59	18.35						
				327.79	151.57	56.60						
ZnO	Rock salt-NM	[0]	DFT	258.13	164.10	85.12	195.45	67.08	180.58	0.35	1.81	0.44
ZnO	Wurtzite-NM	[0]	DFT	204.89	110.98	39.65	150.07	40.39	111.19	0.38	...	0.05
				204.89	125.58	36.98						
				220.11	125.58	36.98						
ESO	PM [160]	[0]	DFT; U = 6	287.00	131.00	87.00	183.00	83.28	216.94	0.30	1.12	0.01
ESO	NM [160]	[0]	DFT; U = 0	303.00	124.00	88.00	183.67	88.60	228.97	0.29	0.98	0.00
ESO	AFM [160]	[0]	DFT; U = 6	274.27	142.70	93.53	186.56	81.23	212.80	0.31	1.42	0.15

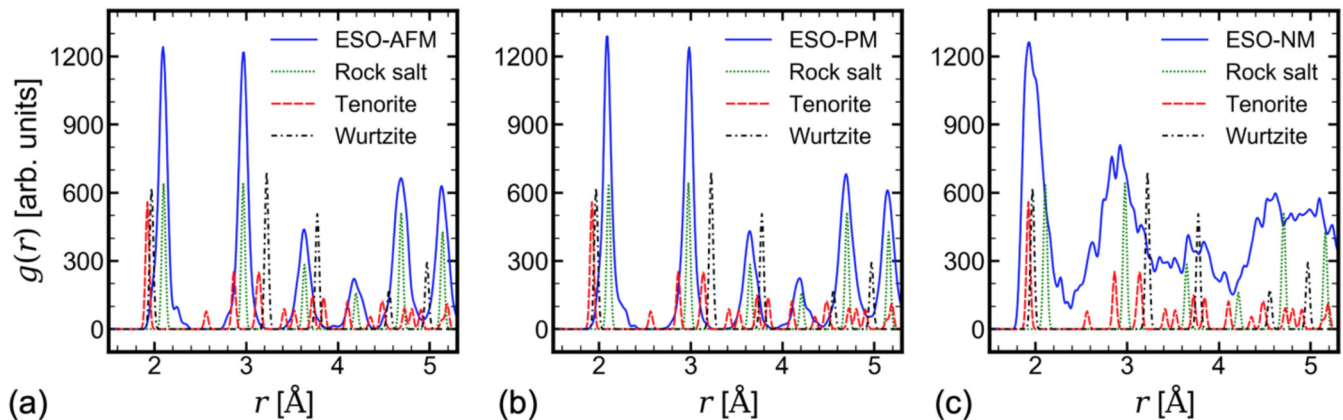


**FIG. 3.** Radial distribution function,  $g(r)$ , is plotted in solid blue line for (a) AFM, (b) PM, and (c) NM structures. For comparison,  $g(r)$  is also plotted for rock salt, tenorite, and wurtzite structures with equivalent lattice constants in dotted green line, dashed red line, and dotted-dashed line, respectively.

First, we examine Zener's anisotropy ratio,  $A^Z$ , for the individual binary oxides. We find that  $A^Z < 1$  for AFM ordered CoO and NiO, and  $A^Z > 1$  for NM MgO, CuO, and ZnO. Consequently, the AFM ordered materials—CoO and NiO—are stiffer toward shearing in the (110) planes along the  $[1, -1, 0]$  direction than shearing in the (100) plane along the  $[0, 1, 0]$  direction. Furthermore, the opposite is true for the NM materials—MgO, CuO, and ZnO—in the rock salt phase, i.e., they are stiffer toward shearing in the (100) planes along the  $[0, 1, 0]$  direction than shearing in the (110) plane along the  $[1, -1, 0]$  direction. Young's modulus for individual binary oxides, along with the AFM, PM, and NM models of ESO, is plotted in Fig. S3 in the [supplementary material](#).

Second, we constructed a disordered unit cell using the SQS approach to study the elastic properties of the ESO. Here, we considered a nonmagnetic phase and two different magnetic phases—AFM ordering similar to ground phases of CoO and NiO as well as a paramagnetic phase. We have considered two different SQS configurations for the paramagnetic phase whose energy difference was within 20 meV. The relaxed structures of all entropy stabilized oxides can be found at the end of the [supplementary material](#). The value of  $A^Z$  for the ESO modeled using AFM, PM, and NM phases are 1.42, 1.12, and 0.98, respectively. We find that the elastic anisotropy of the AFM phase is much stronger than those of the PM and NM phases. This suggests that the elastic anisotropy of the ESO is highly sensitive to its magnetic structure. Specifically, the elastic anisotropy of AFM > PM > NM phases should generally decrease with increasing temperature, due to AFM  $\rightarrow$  PM phase transition. The influence of the magnetic state on the local structure and on the elastic properties is further analyzed through the radial distribution function,  $g(r)$ , and the polar displacements of the cations for each model.

Figure 3 shows  $g(r)$  for (a) the AFM, (b) the lowest energy PM (of the two studied models), and (c) the NM structures, compared to representative  $g(r)$  of rock salt at the ESO lattice constant, tenorite at the CuO lattice constant, and wurtzite at the Zn lattice constant. While there are only minor differences in  $g(r)$  between

the AFM and PM structures, we find significant differences of these structures with the NM structure. Specifically, the first blue peak at  $\sim 2 \text{ \AA}$ —corresponding to the A–O bond distance—aligns with the (dotted green) peak of the rock salt phase for the AFM and PM structures, suggesting pure rock salt character. On the contrary, the first blue peak of the NM structure is broadened with character comprising rock salt, tenorite, and wurtzite structures. This suggests that the presence of local distortions, arising from the tendency of Cu and Zn to form secondary phases, may enhance the isotropy of the material. Furthermore, the similarity between the AFM and PM structures suggests that the decrease in the value of  $A^Z$  between the AFM and PM structures may exclusively be attributed to the strongly anisotropic magnetic interactions in the AFM model. We find similar trends for comparisons of the cation polar displacements (CPD) between the AFM, PM, and NM structures. Figure S4 in the [supplementary material](#) shows the distribution of CPD for all structures. The cation displacements in the AFM and PM structures are small for all cations  $< 0.05 \text{ \AA}$ . However, the cation displacements in the NM structure are substantially large  $\sim 0.5 \text{ \AA}$  for Cu and Zn cations, suggesting a tendency to locally distort to the tenorite and wurtzite structures, respectively. We also find that while Mg displacements are comparatively smaller,  $\sim 0.25 \text{ \AA}$ , Ni and Co are prone to local displacements.

Figure 4 shows a plot of the average bulk modulus vs the average shear modulus for the five constituent binary oxides and the ESO, (Mg, Co, Ni, Cu, Zn)O. Values for the elastic moduli of NiO and CoO were calculated considering AFM ordering and with  $U = 6.0 \text{ eV}$ . The red line in the diagram highlights the boundary established by the largest and smallest average values of the bulk and shear moduli of the constituent binary oxides. It was found that the values predicted for the average moduli of the ESO, in the NM, AFM, and PM magnetic states, fall within these bounds and that these values are comparable to the values calculated using the rule of mixtures (ROM), which is often used as a first approximation to estimate properties, such as the elastic properties, of random solid solutions.<sup>51</sup> While the structure of high-entropy metallic alloys is



different from that of the ESO compound investigated in this paper, it is worth mentioning that many high-entropy alloys have been found to follow this trend,<sup>51,52</sup> although there are exceptions such as NiFeCrCoMn, which is predicted to have a bulk modulus lower than those of its constituents.<sup>52</sup> While alloying effects are known to result in alloys with elastic properties that are lower than those of their constituents, these trends have not been established for either high-entropy alloys or entropy-stabilized oxides.

Also included in Fig. 4 are lines corresponding to different values of Pugh's ratio ( $K/G$ ), including one for  $K/G = 1.75$ , which is widely used to distinguish materials with ductile behavior ( $K/G > 1.75$ ). The results in Fig. 4 suggest that the ESO compound, which has a value of Pugh's ratio—equal to 2.07, 2.20, and 2.30, in the NM, PM, and AFM phases, respectively, should exhibit ductile behavior, which is consistent with the indentation behavior in that no cracks formed at the corners of the indents.

Figure 5 plots the values of  $A^Z$  vs  $A^U$  for the ESO in the AFM, PM, and NM structures. The data for the constituent parent oxides are also shown for comparison. The line  $A^Z = 1$  corresponds to elastic isotropy and separates the plot into two regions: above this line  $c_{44} > \frac{c_{11}-c_{12}}{2}$ , while the opposite case holds below the line. It is worth noting that Zener's anisotropy parameter for the ESO is close to the boundary of the values of the constituent binary oxides

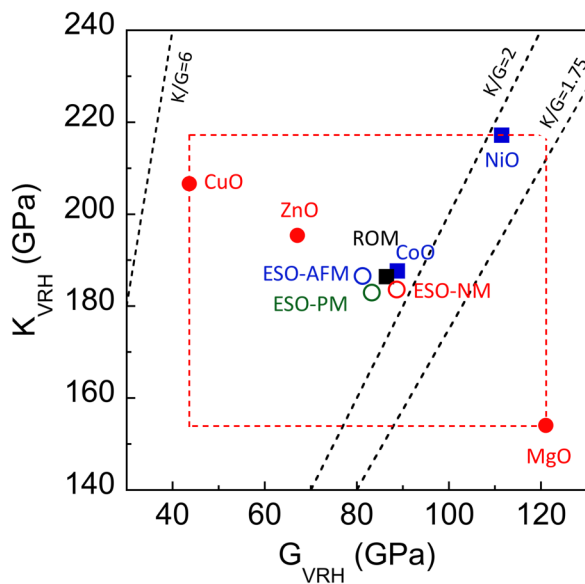


**FIG. 4.** Plot of Voigt–Reuss–Hill average values of bulk vs shear moduli. Data points correspond to values determined from first principles calculations. ROM value shown in black solid square corresponds to values calculated using the rule of mixtures. Red solid circles correspond to values calculated for nonmagnetic binary oxides with  $U = 0.0$  eV. Blue solid squares correspond to values calculated for AFM binary oxides with  $U = 6.0$  eV. Values for the ESO compound are shown with open circles: (i) the red circle for nonmagnetic calculation at  $U = 0.0$  eV, (ii) the green circle is for paramagnetic calculation with  $U = 6.0$  eV, and (iii) the blue circle is for antiferromagnetic calculation with  $U = 6.0$  eV. The dashed red line is used to illustrate bounds provided by the elastic constants of the constituent binary oxides.

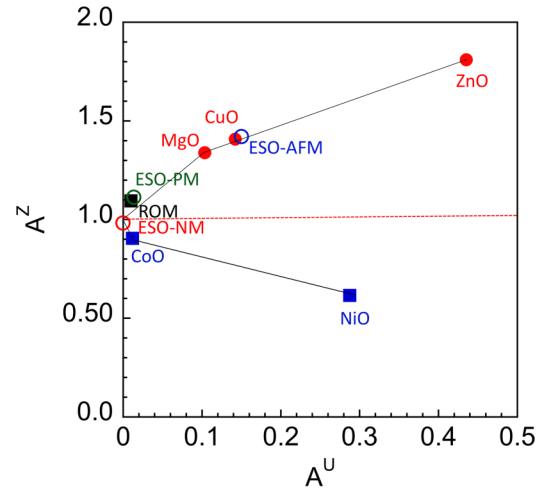


**FIG. 5.** Plot of Zener elastic anisotropy parameter  $A^Z$  vs elastic anisotropy index  $A^U$  for the ESO and its constituent binary oxides. Solid red circles correspond to values determined using  $U = 0.0$  eV for nonmagnetic calculations. Solid blue squares correspond to calculations for CoO and NiO for  $U = 6.0$  eV and considering AFM ordering. Open symbols correspond to values for the ESO compound: (i) the red circle is for NM calculation with  $U = 0.0$  eV, (ii) the green circle is for PM calculation with  $U = 6.0$  eV, and (iii) the blue circle is for AFM calculation with  $U = 6.0$  eV. The black solid lines are used to highlight the boundary set by the constituent binary oxides. The elastic anisotropy values of PM and NM calculations for the ESO compound are approximately equal to the average values (shown in solid black square) obtained from the rule-of mixtures.

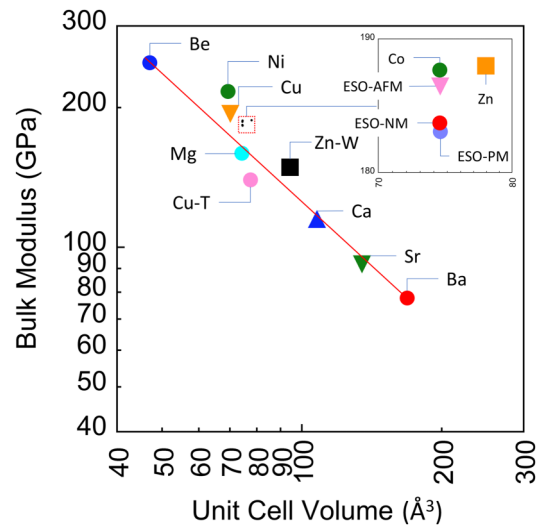


**FIG. 6.** Bulk modulus plotted as a function of unit cell volume plotted on a log–log scale for several divalent binary oxides in rock salt phase including ESO-AFM, ESO-PM, and ESO-NM. CuO and ZnO are plotted in their respective ground phases represented by Cu-T (tenorite) and Zn-W (wurtzite). Inset shows the data points clustered near CuO.

and that an average of these values yields 1.04 (represented in the plot as ROM), which is very close to the value determined from first principles calculations (0.98). The calculated value of the elastic anisotropy index,  $A^U$ , for the ESO was found to be effectively zero ( $3.4 \times 10^{-4}$ ), which is representative of a material with high elastic isotropy. Conversely, for the ESO in the paramagnetic phase (which is stable at  $T = RT$ ),  $A^Z = 1.12$ , indicating a mild degree of elastic anisotropy, which further increases to  $A^Z = 1.42$  for the low temperature AFM phase, indicating enhanced anisotropy.

Finally, we analyze the bulk modulus of the ESO through the well-known relation between the unit cell volume and bulk modulus in ionic solids.<sup>53,54</sup> Figure 6 plots the VRH-averaged bulk modulus as a function of the unit cell volume for several divalent binary oxides in the rock salt phase, including ESO-AFM, ESO-PM, and ESO-NM. We find that the bulk constants of ESO in the AFM, PM, and NM structures follow the general trend dictated by the binary oxides of the divalent cations.

#### IV. CONCLUSIONS

The elastic constants of the multi-component oxide (Mg, Co, Ni, Cu, Zn)O were determined from first principles calculations and experimental indentation measurements. The values of indentation modulus at ambient conditions revealed a high degree of elastic isotropy. Predictions using first principles calculations confirmed a high degree of isotropy for a nonmagnetic structure with  $A^Z = 0.98$  and slightly increases for a paramagnetic structure  $A^Z = 1.12$ . Conversely, the low temperature antiferromagnetic phase has a higher degree of anisotropy,  $A^Z = 1.42$ . Comparisons of the AFM, PM, and NM structures indicate two complementary contributions, influencing the isotropy. First, the uncorrelated magnetic state promotes isotropy, which can be further amplified by inclusion of local wurtzite and tenorite structures. Interestingly, we find that the bulk and shear moduli of the multicomponent oxide are within the boundaries set by the constituent oxides and close to the values predicted by the rule of mixtures. Computational data and experimental observations indicate that the ESO should exhibit ductile behavior, which would make it an attractive candidate for engineering applications.

#### SUPPLEMENTARY MATERIAL

See the [supplementary material](#) for details about the characterization of the material using electron backscatter diffraction and nanoindentation, and procedures for analyzing the indentation of a surface with a given crystallographic orientation, and the method used for determining the elastic constants from DFT.

#### ACKNOWLEDGMENTS

Research sponsored by the Laboratory Directed Research and Development Program of Oak Ridge National Laboratory, managed by UT-Battelle, LLC, for the U.S. Department of Energy (DOE). The authors acknowledge the computational resources at NERSC and their colleagues Christopher Fancher and Raphael P. Hermann of ORNL for reviewing the manuscript. De Xin Chen participated in this project through a Mickey Leland Energy Fellowship (MLEF)

internship at the Oak Ridge National Laboratory while he was an undergraduate student at the Massachusetts Institute of Technology. The MLEF program is funded by the Fossil Energy Program at the U.S. Department of Energy Program and managed by Oak Ridge Associated Universities. The authors thank Professor Trudy Kriven and David Tseng of KeaneTech, LLC, for preparing and selling a special order of ESO powders according to their patented steric entrapment method.

This manuscript has been authored by UT-Battelle, LLC, under Contract No. DE-AC05-00OR22725 with the U.S. Department of Energy. The United States Government retains and the publisher, by accepting the article for publication, acknowledges that the United States Government retains a non-exclusive, paid-up, irrevocable, world-wide license to publish or reproduce the published form of this manuscript, or allow others to do so, for United States Government purposes. DOE will provide public access to these results of federally sponsored research in accordance with the DOE Public Access Plan (<http://energy.gov/downloads/doe-public-access-plan>).

#### DATA AVAILABILITY

The data that support the findings of this study are available within the article and its [supplementary material](#). Additional data are available from the corresponding author upon reasonable request.

#### REFERENCES

- <sup>1</sup>H. Olijnyk and A. P. Jephcoat, *Solid State Commun.* **115**, 335 (2000).
- <sup>2</sup>A. Schmitz, M. Chandrasekaran, G. Ghosh, and L. Delaey, *Acta Metall.* **37**, 3151 (1989).
- <sup>3</sup>X. Han, N. M. Ghoniem, and Z. Wang, *Philos. Mag.* **83**, 3705 (2003).
- <sup>4</sup>V. Tvergaard and J. W. Hutchinson, *J. Am. Ceram. Soc.* **71**, 157 (1988).
- <sup>5</sup>J. Brugués, J. Ignés-Mullol, J. Casademunt, and F. Sagués, *Phys. Rev. Lett.* **100**, 037801 (2008).
- <sup>6</sup>C. M. Rost, E. Sachet, T. Borman, A. Moballeghe, E. C. Dickey, D. Hou, J. L. Jones, S. Curtarolo, and J.-P. Maria, *Nat. Commun.* **6**, 8485 (2015).
- <sup>7</sup>Y. Sharma, B. L. Musico, X. Gao, C. Hua, A. F. May, A. Herklotz, A. Rastogi, D. Mandrus, J. Yan, H. N. Lee, M. F. Chisholm, V. Keppens, and T. Z. Ward, *Phys. Rev. Mater.* **2**, 060404 (2018).
- <sup>8</sup>A. Sarkar, R. Djenadic, D. Wang, C. Hein, R. Kautenburger, O. Clemens, and H. Hahn, *J. Eur. Ceram. Soc.* **38**, 2318 (2018).
- <sup>9</sup>S. Jiang, T. Hu, J. Gild, N. Zhou, J. Nie, M. Qin, T. Harrington, K. Vecchio, and J. Luo, *Scr. Mater.* **142**, 116 (2018).
- <sup>10</sup>K. Chen, X. Pei, L. Tang, H. Cheng, Z. Li, C. Li, X. Zhang, and L. An, *J. Eur. Ceram. Soc.* **38**, 4161 (2018).
- <sup>11</sup>J. Gild, M. Samiee, J. L. Braun, T. Harrington, H. Vega, P. E. Hopkins, K. Vecchio, and J. Luo, *J. Eur. Ceram. Soc.* **38**, 3578 (2018).
- <sup>12</sup>J. Dąbrowa, M. Stygar, A. Mikula, A. Knapik, K. Mrocza, W. Tejchman, M. Danielewski, and M. Martin, *Mater. Lett.* **216**, 32 (2018).
- <sup>13</sup>J. Gild, Y. Zhang, T. Harrington, S. Jiang, T. Hu, M. C. Quinn, W. M. Mellor, N. Zhou, K. Vecchio, and J. Luo, *Sci. Rep.* **6**, 37946 (2016).
- <sup>14</sup>E. Castle, T. Csanádi, S. Grasso, J. Dusza, and M. Reece, *Sci. Rep.* **8**, 8609 (2018).
- <sup>15</sup>J. Dusza, P. Švec, V. Girman, R. Sedlák, E. G. Castle, T. Csanádi, A. Kovalčíková, and M. J. Reece, *J. Eur. Ceram. Soc.* **38**, 4303 (2018).
- <sup>16</sup>X. Yan, L. Constantin, Y. Lu, J.-F. Silvain, M. Nastasi, and B. Cui, *J. Am. Ceram. Soc.* **101**, 4486 (2018).
- <sup>17</sup>J. Zhou, J. Zhang, F. Zhang, B. Niu, L. Lei, and W. Wang, *Ceram. Int.* **44**, 22014 (2018).
- <sup>18</sup>P. Sarker, T. Harrington, C. Toher, C. Oses, M. Samiee, J.-P. Maria, D. W. Brenner, K. S. Vecchio, and S. Curtarolo, *Nat. Commun.* **9**, 4980 (2018).

- <sup>19</sup>J. Zhang, J. Yan, S. Calder, Q. Zheng, M. A. McGuire, D. L. Abernathy, Y. Ren, S. H. Lapidus, K. Page, H. Zheng, J. W. Freeland, J. D. Budai, and R. P. Hermann, *Chem. Mater.* **31**, 3705 (2019).
- <sup>20</sup>A. Sarkar, L. Velasco, D. Wang, Q. Wang, G. Talasila, L. de Biasi, C. Kübel, T. Brezesinski, S. S. Bhattacharya, H. Hahn, and B. Breitung, *Nat. Commun.* **9**, 3400 (2018).
- <sup>21</sup>P. B. Meisenheimer, T. J. Kratočil, and J. T. Heron, *Sci. Rep.* **7**, 13344 (2017).
- <sup>22</sup>C. Zener, *Elasticity and Anelasticity of Metals* (University of Chicago Press, 1948).
- <sup>23</sup>T. S. Duffy, *Am. Mineral.* **103**, 977 (2018).
- <sup>24</sup>D. Legut, M. Friák, and M. Šob, *Phys. Rev. Lett.* **99**, 016402 (2007).
- <sup>25</sup>S. I. Ranganathan and M. Ostojca-Starzewski, *Phys. Rev. Lett.* **101**, 055504 (2008).
- <sup>26</sup>M. A. Gülgün, W. M. Kriven, and M. H. Nguyen, U.S. Patent 6,482,387 (19 November 2002).
- <sup>27</sup>J. J. Vlassak and W. D. Nix, *J. Mech. Phys. Solids* **42**, 1223 (1994).
- <sup>28</sup>Z. Hashin, *J. Appl. Mech.* **50**, 481 (1983).
- <sup>29</sup>G. Kresse and J. Furthmüller, *Comput. Mater. Sci.* **6**, 15 (1996).
- <sup>30</sup>G. Kresse and J. Furthmüller, *Phys. Rev. B* **54**, 11169 (1996).
- <sup>31</sup>J. P. Perdew, A. Ruzsinszky, G. I. Csonka, O. A. Vydrov, G. E. Scuseria, L. A. Constantin, X. Zhou, and K. Burke, *Phys. Rev. Lett.* **100**, 136406 (2008).
- <sup>32</sup>P. E. Blöchl, *Phys. Rev. B* **50**, 17953 (1994).
- <sup>33</sup>G. Kresse and D. Joubert, *Phys. Rev. B* **59**, 1758 (1999).
- <sup>34</sup>S. L. Dudarev, G. A. Botton, S. Y. Savrasov, C. J. Humphreys, and A. P. Sutton, *Phys. Rev. B* **57**, 1505 (1998).
- <sup>35</sup>A. Zunger, S.-H. Wei, L. G. Ferreira, and J. E. Bernard, *Phys. Rev. Lett.* **65**, 353 (1990).
- <sup>36</sup>A. van de Walle, P. Tiwary, M. de Jong, D. L. Olmsted, M. Asta, A. Dick, D. Shin, Y. Wang, L.-Q. Chen, and Z.-K. Liu, *Calphad* **42**, 13 (2013).
- <sup>37</sup>A. Jain, S. P. Ong, G. Hautier, W. Chen, W. D. Richards, S. Dacek, S. Cholia, D. Gunter, D. Skinner, G. Ceder, and K. A. Persson, *APL Mater.* **1**, 011002 (2013).
- <sup>38</sup>M. de Jong, W. Chen, T. Angsten, A. Jain, R. Notestine, A. Gamst, M. Sluiter, C. Krishna Ande, S. van der Zwaag, J. J. Plata, C. Toher, S. Curtarolo, G. Ceder, K. A. Persson, and M. Asta, *Sci. Data* **2**, 150009 (2015).
- <sup>39</sup>C. Kittel, *Introduction to Solid State Physics* (John Wiley & Sons Inc., 2004).
- <sup>40</sup>B. X. Yang, J. M. Tranquada, and G. Shirane, *Phys. Rev. B* **38**, 174 (1988).
- <sup>41</sup>M. Radovic, E. Lara-Curzio, and L. Riestler, *Mater. Sci. Eng. A* **368**, 56 (2004).
- <sup>42</sup>P. Gopal and N. A. Spaldin, *J. Electron. Mater.* **35**, 538 (2006).
- <sup>43</sup>A. J. Cinthia, R. Rajeswarapalanichamy, and K. Iyakutti, *Z. Naturforsch. A* **70**, 797 (2015).
- <sup>44</sup>D. Isaak, O. Anderson, and T. Goto, *Phys. Chem. Miner.* **16**, 704 (1989).
- <sup>45</sup>Y. Sumino, M. Kumazawa, O. Nishizawa, and W. Pluschkell, *J. Phys. Earth* **28**, 475 (1980).
- <sup>46</sup>P. de V Du Plessis, S. J. van Tonder, and L. Alberts, *J. Phys. C Solid State Phys.* **4**, 1983 (1971).
- <sup>47</sup>N. Uchida and S. Saito, *J. Acoust. Soc. Am.* **51**, 1602 (1972).
- <sup>48</sup>M. D. Towler, N. L. Allan, N. M. Harrison, V. R. Saunders, W. C. Mackrodt, and E. Aprà, *Phys. Rev. B* **50**, 5041 (1994).
- <sup>49</sup>W. Jifang, E. S. Fisher, and M. H. Manghnazmi, *Chinese Phys. Lett.* **8**, 153 (1991).
- <sup>50</sup>K. H. Max Born, *Dynamical Theory of Crystal Lattices* (OUP, 1998).
- <sup>51</sup>S. Huang, F. Tian, and L. Vitos, *J. Mater. Res.* **33**, 2938 (2018).
- <sup>52</sup>M. C. Gao, J.-W. Yeh, P. K. Liaw, and Y. Zhang, *High-Entropy Alloys* (Springer International Publishing, 2016).
- <sup>53</sup>P. K. Lam, M. L. Cohen, and G. Martinez, *Phys. Rev. B* **35**, 9190 (1987).
- <sup>54</sup>M. L. Cohen, *Phys. Rev. B* **32**, 7988 (1985).